Opto-Electronic Advances

ISSN 2096-4579 CN 51-1781/TN

Vortex-field enhancement through high-threshold geometric metasurface

Qingsong Wang, Yao Fang, Yu Meng, Han Hao, Xiong Li, Mingbo Pu, Xiaoliang Ma and Xiangang Luo

Citation: Wang QS, Fang Y, Meng Y, et al. Vortex-field enhancement through high-threshold geometric metasurface. *Opto-Electron Adv* **7**, 240112(2024).

https://doi.org/10.29026/oea.2024.240112

Received: 14 May 2024; Accepted: 12 July 2024; Published online: 10 September 2024

Related articles

Resonantly enhanced second- and third-harmonic generation in dielectric nonlinear metasurfaces
Ji Tong Wang, Pavel Tonkaev, Kirill Koshelev, Fangxing Lai, Sergey Kruk, Qinghai Song, Yuri Kivshar, Nicolae C. Panoiu
Opto-Electronic Advances 2024 **7**, 230186 doi: 10.29026/oea.2024.230186

Miniature tunable Airy beam optical meta-device
Jing Cheng Zhang, Mu Ku Chen, Yubin Fan, Qinmiao Chen, Shufan Chen, Jin Yao, Xiaoyuan Liu, Shumin Xiao, Din Ping Tsai
Opto-Electronic Advances 2024 **7**, 230171 doi: 10.29026/oea.2024.230171

Functionality multiplexing in high-efficiency metasurfaces based on coherent wave interferences
Yuejiao Zhou, Tong Liu, Changhong Dai, Dongyi Wang, Lei Zhou
Opto-Electronic Advances 2024 **7**, 240086 doi: 10.29026/oea.2024.240086

More related article in Opto-Electronic Journals Group website

OEA Opto-Electronic Advances

http://www.oejournal.org/oea

OE_Journal @OptoElectronAdv

Opto-Electronic Advances

Article

December 2024, Vol. 7, No. 12

DOI: 10.29026/oea.2024.240112 CSTR: 32247.14.oea.2024.240112

Vortex-field enhancement through high-threshold geometric metasurface

Qingsong Wang[1,2†], Yao Fang[1,2†], Yu Meng[1,2], Han Hao[1,2,3], Xiong Li[1,2,3*], Mingbo Pu[1,2,3,4], Xiaoliang Ma[1,2,3] and Xiangang Luo[1,2,3*]

Intense vortex beam is expected to empower captivating phenomena and applications in high power laser-matter interactions. Currently, the superposition of multiple vortex beams has shown the unique ability to tailor and enhance the vortex field. However, traditional strategies to generate such beams suffer from large volume or/and low laser-induced damage threshold, hindering the practical widespread applications. Herein, a single high-threshold metasurface is proposed and experimentally demonstrated for the generation and superposition of multiple collinear vortex beams. This scheme takes advantage of the high conversion efficiency of phase-only modulation in the metasurface design by adopting the concept of a sliced phase pattern in the azimuthal direction. An optical hot spot with an enhanced intensity and steady spatial propagation is experimentally achieved. Moreover, femtosecond laser-induced birefringent nanostructures embedded in silica glass are utilized as the building block with high optical efficiency. Transmittance greater than 99.4% in the near-infrared range and laser-induced damage threshold as high as 68.0 J/cm^2 (at 1064 nm, 6 ns) are experimentally verified. Considering these remarkable performances, the demonstrated high-threshold metasurface has promising applications in a host of high-power laser fields.

Keywords: multiple vortex beams; metasurface; high-threshold; birefringent nanostructures; femtosecond laser

Wang QS, Fang Y, Meng Y et al. Vortex-field enhancement through high-threshold geometric metasurface. *Opto-Electron Adv* **7**, 240112 (2024).

Introduction

Optical vortex beam, carrying orbital angular momentum (OAM), is characterized with helical wavefront and donut-like intensity cross-section[1–4]. High-intensity vortex beam is desired in numerous fundamental investigations and applications of laser-matter interactions in terms of nonlinear optical effects[5], terahertz vortex wave generation[6], laser ablation and material processing[7], and beyond. However, the emission power of a single OAM beam is limited at present. Recently, the superposition of multiple vortex beams has shown the unique ability to tailor and enhance the vortex field. In principle, vortex beams carrying different OAMs are mutually orthogonal, providing the spatial modal basis set to generate a beam with space-dependent intensity[8–10]. Especially, by engineering the spatial-variant interference effect

[1]National Key Laboratory of Optical Field Manipulation Science and Technology, Chinese Academy of Sciences, Chengdu 610209, China; [2]State Key Laboratory of Optical Technologies on Nano-Fabrication and Micro-Engineering, Institute of Optics and Electronics, Chinese Academy of Sciences, Chengdu 610209, China; [3]College of Materials Science and Opto-Electronic Technology, University of Chinese Academy of Sciences, Beijing 100049, China; [4]Research Center on Vector Optical Fields, Institute of Optics and Electronics, Chinese Academy of Sciences, Chengdu 610209, China.

†These authors contributed equally to this work.

*Correspondence: X Li, E-mail: lixiong@ioe.ac.cn; XG Luo, E-mail: lxg@ioe.ac.cn

Received: 14 May 2024; Accepted: 12 July 2024; Published online: 10 September 2024

Open Access This article is licensed under a Creative Commons Attribution 4.0 International License.
To view a copy of this license, visit http://creativecommons.org/licenses/by/4.0/.

© The Author(s) 2024. Published by Institute of Optics and Electronics, Chinese Academy of Sciences.

(constructive or destructive interference) with multiple collinear vortex beams (MCVBs), light can be confined to a smaller area[11]. As a result, the localized optical intensity is significantly enhanced.

The MCVBs can be traditionally generated by the combination of multiple optical systems involving vortex beam generation and collinear superposition. The optical setup is complex and has a bulky volume, which is impractical for compact and miniaturized applications. Another main method to generate the MCVBs is based on spatial light modulators (SLMs)[11–13], which reduce the system volume to a certain extent, but generally suffer from low resolution. Moreover, low laser-induced damage threshold (LIDT) is another critical issue for typical SLMs, which limits the applications mainly in the fields of low laser power. When irradiated with high-power laser, thermal or nonthermal loading can lead to irreversible damage to the SLMs and thereby deteriorating the optical performance, which is the challenge for typical SLMs to be applied in high-power laser systems.

Optical metasurfaces aided by the rapid advances in nanofabrication provide an alternative approach to address these shortcomings. With the development of propagation phase[14], generalized geometric phase[15], asymmetric spin orbit interaction[16], and catenary optics[17], metasurfaces allow the arbitrary modulation of the phase, amplitude, and polarization of the incident beam with micro- and nanoscale[18,19]. These unprecedented abilities open up a way for the miniaturization and integration of optical elements and systems. Numerous optical elements and versatile functionalities have been realized including metalenses[20–23], optical holograms[24–26], optical detection[27–29], structured beam generation[30–33], optical encryption[34–36], and beyond. Recently, metasurfaces have been employed to generate and overlap the multiple vortex beams[37–39]. For example, Ming et al. have demonstrated the creation and manipulation of optical singularity structures by leveraging the superposition of multiple Laguerre-Gaussian modes with a single geometric metasurface[39]. Additionally, a LIDT of 1.1 J/cm^2 (at 532 nm, 5 ns) has been recently verified for titanium dioxide-based metasurface[40]. Nevertheless, it is worth noting that low LIDT is still a critical issue for metasurfaces, which is related to the intrinsically low damage threshold of the constituent materials and the local field enhancement effect during light-matter interactions. In the past few years, emerging femtosecond laser-induced form birefringence, known as a generalized metasurface[41–43], has provided fascinating opportunities for manipulating light with high transmittance and high LIDT[44,45].

In this work, to overcome the aforementioned limitations of the MCVBs generation for enhancing the vortex field, a single geometric metasurface with high LIDT is proposed and experimentally demonstrated based on femtosecond laser-induced form birefringence embedded in silica glass. The metasurface is designed by adopting the concept of a sliced phase pattern in the azimuthal direction, generating the MCVBs with equally spaced topological charge (l) for orthogonal-mode superposition. Optical hot spots with enhanced intensity and steady spatial propagation can be realized and modulated. As a proof of the concept, a single optical hot spot with an intensity gain larger than 3.4 within a propagation distance of 1 m is experimentally demonstrated and compared with calculation values. Benefiting from the nanoscale features in the laser-induced form birefringence, transmittance greater than 99.4% in the near-infrared range and LIDT as high as 68.0 J/cm^2 (at 1064 nm, 6 ns) are experimentally verified. The demonstrated high-threshold metasurface has promising applications in a host of high-power laser fields.

Results and discussion

Principle and design of metasurface

Figure 1(a) illustrates the schematic diagram of the metasurface designed for the generation and superposition of MCVBs. Unlike conventional methods that encode both amplitude and phase onto a phase-only filter simultaneously at the cost of conversion efficiency, our approach focuses solely on phase modulation. This is known as the phase-only modulation strategy, which is achieved by employing the concept of a sliced phase pattern in the azimuthal direction[46]. As a Gaussian beam with circular polarization traverses the metasurface, MCVBs featuring equally spaced OAM charge number are generated. Additionally, the vortex field can be enhanced owing to the superposition effect.

Similar to previous work aimed at generating a pure single OAM channel, the sliced phase pattern modulates the phase of the output beam in the azimuthal direction. However, there is a crucial difference in the evolution of the azimuthal angle (α)-dependent phase. While a continuous spiral phase ($l\alpha$) is applied for generating a pure single OAM, the sliced phase pattern comprises variant

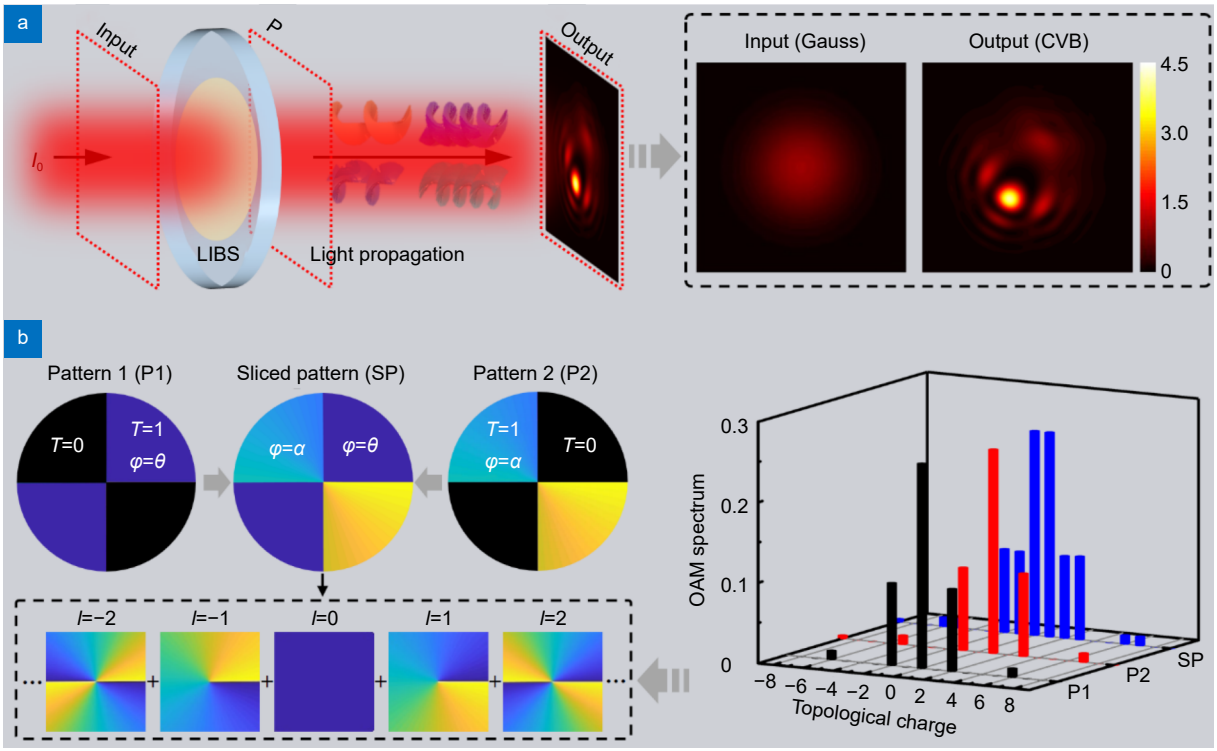

Fig. 1 | (**a**) Schematic diagram of the metasurface for the generation and superposition of MCVBs. OAM components with equally spaced topological charge (*l*) are encoded within the output beam. LIBS: laser induced birefringent structure. The output light is confined with higher localized optical intensity due to the superposition effect. (**b**) Illustrate of the principle for MCVBs generation based on a sliced phase pattern in the azimuthal direction. Two-fold rotational symmetry (*N*=2), l_1=0, and l_2=1 are chosen for example. And θ is an initial phase delay that can be optimized to modify the properties of MCVBs, such as the OAM spectrum, for maximizing the intensity gain.

truncated spiral phases within different angular apertures with rotational symmetry. Figure 1(b) illustrates the principle behind the generation of MCVBs. The sliced phase pattern can be divided into M sets of angular transmission apertures, considering the N-fold rotational symmetry of the topological charge [M=2, N=2 in Fig. 1(b)]. Each set of angular apertures exhibits a spiral phase with pre-defined topological charges (l_1, l_2, …, l_M). When illuminated by a Gaussian beam, the m^{th} set of angular apertures redistributes the laser energy to OAM components with equally spaced topological charges l_m+kN (k is an integer, k=0, ±1, ±2,…). The power proportion of these OAM components, known as the OAM spectrum, is derived from helical harmonic decomposition[47–49], as depicted in Fig. 1(b). By combining the phase patterns of angular transmission apertures, MCVBs can be obtained.

Following the approach for generating MCVBs, the phase of the metasurface is tailored to achieve localized optical intensity enhancement over a specific distance. The configuration of angular transmission apertures, the fold of rotational symmetry, the assigned topological charge within each angular aperture set, and the initial phase delay collectively govern optical intensity modulation. To illustrate this concept, a sliced phase pattern featuring 3 sets of angular apertures and one-fold rotational symmetry is demonstrated. This configuration is depicted in Fig. 2(b), where the azimuthal phase distribution is represented as:

$$\varphi(\alpha)=\begin{cases}0 & \alpha\in[0,2\pi/3)\\ 3\alpha+\beta_1 & \alpha\in[2\pi/3,4\pi/3)\\ -3\alpha+\beta_2 & \alpha\in[4\pi/3,2\pi)\end{cases}, \qquad (1)$$

where β_1 and β_2 are the initial phase delays between adjacent apertures. The intensity distribution of output-modified light at a certain distance z is calculated using Kirchhoff diffraction theory, with a chosen wavelength of 808 nm. The parameters β_1 and β_2 in Eq. (1) can be delicately optimized to maximize the intensity gain which is defined as the ratio of the peak intensity obtained with the sliced phase pattern to that of the Gaussian beam. Figure 2(a) illustrates the evolution of intensity gain at z=1 m relative to the initial phase delays β_1 and β_2. An intensity gain of 4.1 is achieved for β_1=0 and β_2=0.

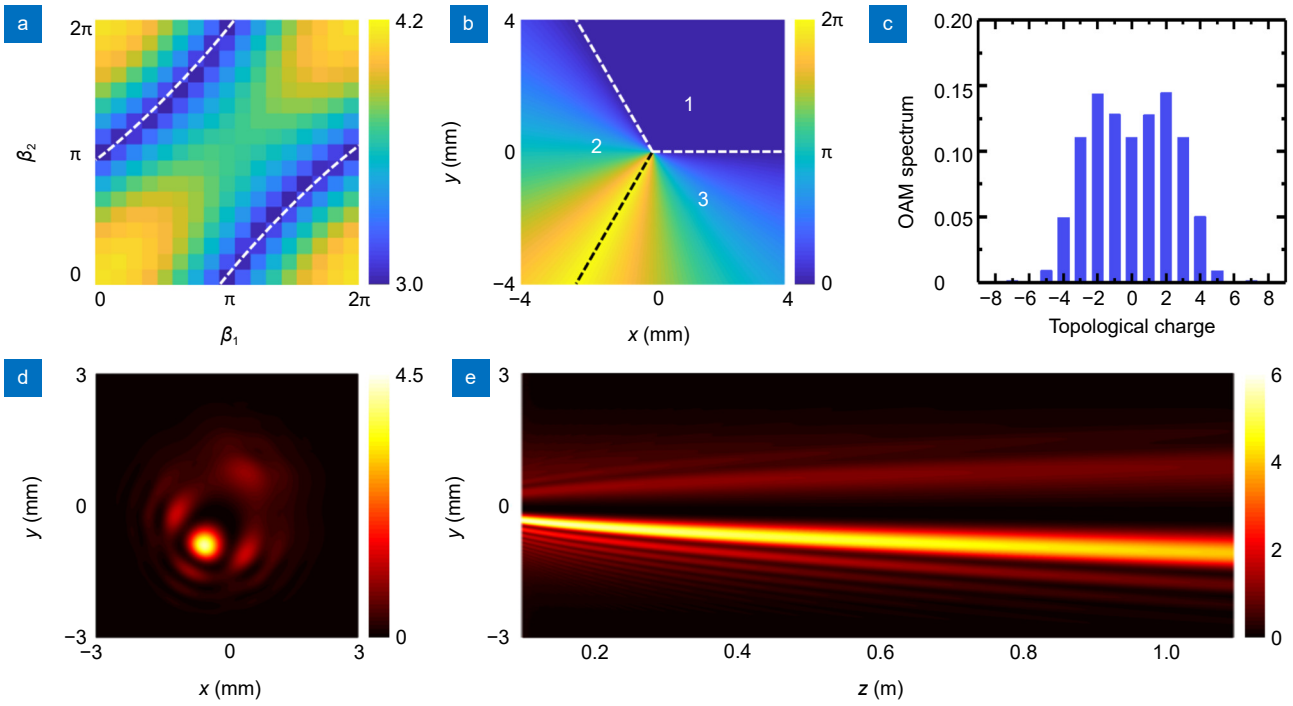

Fig. 2 | Design of the metasurface phase based on a sliced phase pattern in the azimuthal direction. (**a**) Evolution of intensity gain at z=1 m with respect to the initial phase delays β_1 and β_2. (**b**–**d**) Phase profile of the desired metasurface, OAM spectrum, and intensity distribution at a distance of 1 m for β_1=0 and β_2=0. (**e**) Intensity distribution along the propagation direction for β_1=0 and β_2=0. The intensity distribution is normalized to the maximum intensity of the Gaussian beam along the propagation direction.

Correspondingly, the phase profile of the desired metasurface and OAM spectrum of the modulated beam are displayed in Fig. 2(b) and Fig. 2(c), respectively. Analysis reveals that OAMs with topological charges ranging from −4 to 4 are the main orthogonal modes utilized in constructing this beam. A single off-centered hot spot is observed in the intensity profile due to the constructive interference of the modulated beam, as shown in Fig. 2(d). As a comparison, lower intensity gains for cases indicated by white dotted lines in Fig. 2(a) are attributed to the generation of two hot spots in the intensity profile, as depicted in Fig. S1 (Supplementary information). Additionally, the intensity distribution of the modulated beam along the propagation direction is calculated, as shown in Fig. 2(e). Similar intensity profiles at different distances can be identified, which exhibit gradually decreased intensity gain and increased off-centered distance due to the diffraction effect. A more detailed investigation of the evolution of the superposed vortex field with respect to the sliced phase pattern combining different topological charges and initial phase delays is indicated in Supplementary information (see Section 1).

Laser-induced form birefringence nanostructures are harnessed to accomplish geometric phase modulation within the metasurface. These nanostructures can work just as subwavelength uniaxial form-birefringent crystals. When circularly polarized light illuminates these structures, a cross-polarized beam with opposite handedness is generated with an additional geometric phase of $-2\sigma\theta_1$ due to the photonic spin-orbit interaction[15,16,50], where θ_1 represents the azimuthal angle of the birefringent nanostructure controlled by the laser polarization direction, and σ=±1 denotes right-handed and left-handed circularly polarized beams, respectively. The conversion efficiency can be expressed as $\sin^2(\gamma/2)$ without considering the optical loss of subwavelength structures, where γ is the phase retardance between the fast and slow axes. Therefore, to fabricate a metasurface with high conversion efficiency, the parameters of femtosecond laser ablation must be optimized to achieve a phase retardance of π. Additionally, the azimuthal angle of laser-induced form birefringence nanostructures is adjusted in accordance with the designed phase profile.

Laser-induced form birefringence

The experimental setup for fabricating femtosecond laser-induced form birefringence within silica glass (Corning 7980) is outlined in Fig. S5 (Supplementary

information). Rectangular-modified regions were built by scanning a focused femtosecond laser in parallel lines, with an interval of 1 μm. More details regarding this fabrication system are provided in *Materials and methods*. Laser-induced form birefringence primarily arises from the nonlinear energy deposition of ultrafast laser pulses, making it highly dependent on laser writing parameters such as pulse duration, pulse density, pulse energy, and more. Figure 3(a) illustrates the angle of the fast axis, intensity, and retardance of femtosecond laser-modified regions under varying pulse durations, with a constant pulse energy of 1.1 μJ, pulse density of 33 pulses/μm, and laser polarization direction of 0°. The image of the fast axis angle indicates the generation of anisotropic nanostructures when the pulse duration exceeds 350 fs. The fast axis direction of the laser-induced anisotropic nanostructures is parallel to the laser polarization direction. Moreover, a range of nanostructure types, from

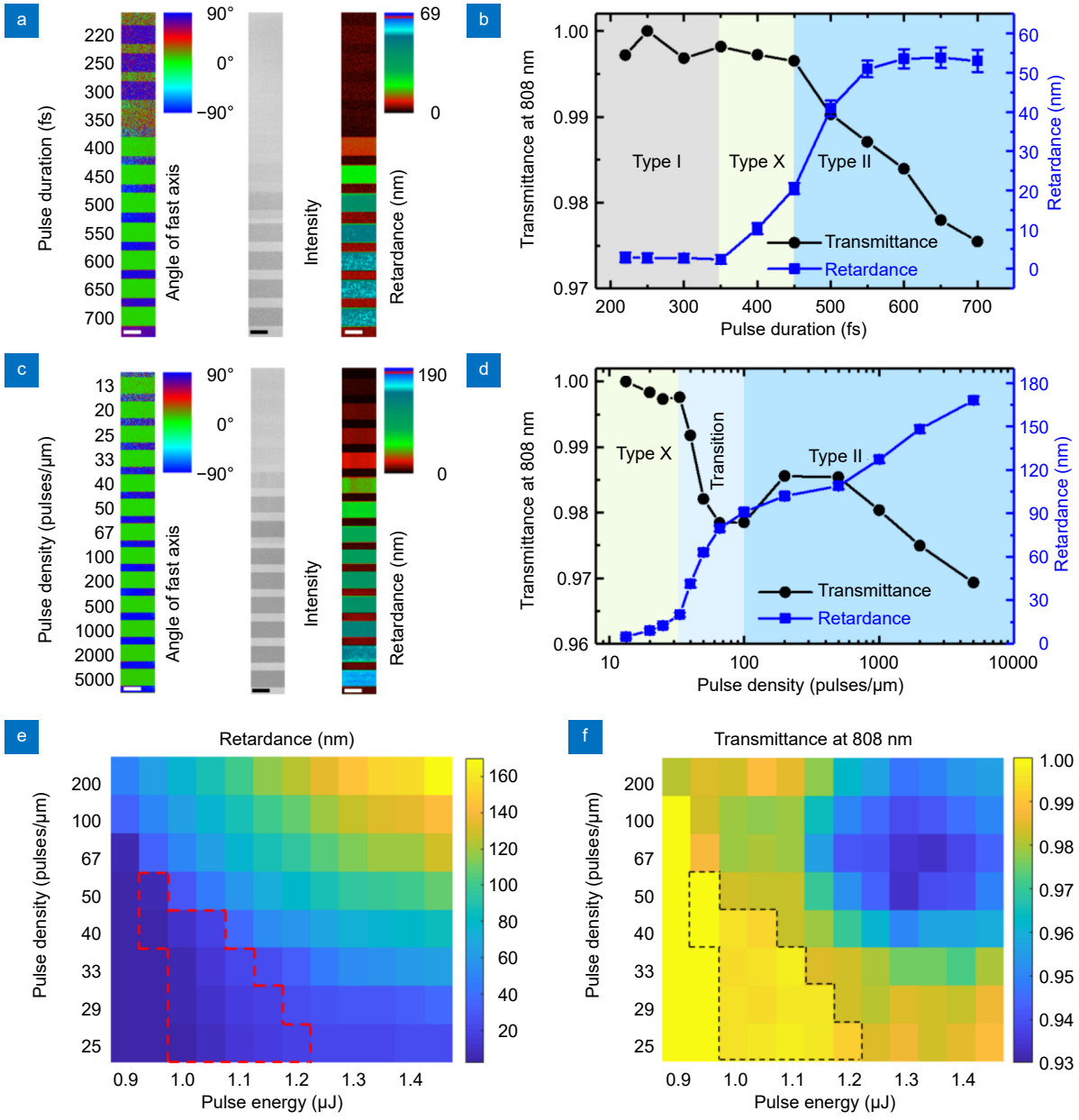

Fig. 3 | Laser-induced form birefringence with different pulse durations, pulse densities, and pulse energies. (**a**, **c**) Angle of the fast axis, intensity, and retardance image of laser-modified regions induced by different pulse durations and pulse densities, respectively. (**b**, **d**) Dependence of transmittance and retardance of laser-modified regions on pulse duration and pulse density, respectively. (**e**, **f**) Pseudo color maps of retardance and transmittance of laser-modified regions induced by different pulse energies and pulse densities. The birefringence was characterized at a wavelength of 655 nm, and the transmittance was measured at a wavelength of 808 nm.

isotropic to birefringent modifications, is discerned by quantitative measurement of the birefringence and transmittance, as depicted in Fig. 3(b). For pulse durations no more than 350 fs, modified regions exhibit ultra-high transmittance, and form birefringence is scarcely discernible as retardance approaches zero. UV-VIS absorption spectra further indicate the presence of laser-induced defects within silica glass (refer to Fig. S6, Supplementary information), suggesting the generation of isotropic (referred to as type I) modification for shorter pulse durations[51]. As pulse duration surpasses 350 fs, birefringent modification becomes apparent, showcasing significant duration-dependent retardance and transmittance, revealing two distinct forms of birefringence. For pulse durations ranging between 350 fs and 450 fs, ultralow-loss birefringence (referred to as type X) is achieved, characterized by a considerable increase in retardance with minimal impact on transmittance, approaching 100%. Consequently, longer pulse durations prove advantageous for enhancing the processing efficiency of ultralow-loss type X metasurfaces. Beyond 450 fs, nanogratings (referred to as type II) emerge within the laser-modified region. The retardance of type II initially increases before stabilizing, while transmittance experiences a rapid decline with longer pulse durations. Type II exhibits higher retardance but lower transmittance compared to type X. In principle, both type X and type II modifications can be utilized to fabricate metasurfaces. However, there is a significant disparity in transmittance, particularly for metasurfaces comprising multiple layers.

Typically, the formation of birefringent nanostructures within transparent materials stems from the cumulative effect of multiple laser pulses. Consequently, pulse density plays a pivotal role in shaping the birefringent properties of laser-modified regions, as illustrated in Fig. 3(c) and Fig. 3(d). Across a pulse density range of 13 to 5000 pulses/μm, with a fixed pulse duration of 450 fs and pulse energy of 1.1 μJ, it becomes evident that the angle of the fast axis remains aligned parallel to the laser polarization direction irrespective of the applied pulse density. However, both retardance and transmittance exhibit significant dependencies on pulse density. As pulse density increases, transmittance undergoes four distinct phases: initially remaining constant (13–33 pulses/μm), followed by a decrease (33–100 pulses/μm), then an increase (100–500 pulses/μm), and finally another decrease (500–5000 pulses/μm). Conversely, retardance demonstrates a straightforward positive correlation with pulse density. Based on the evolution of transmittance and retardance concerning pulse density, three distinct types of birefringent modification emerge: (I) type X for pulse densities up to 33 pulses/μm, (II) a transitional phase for pulse densities ranging from 33 to 100 pulses/μm, and (III) type II for pulse densities exceeding 100 pulses/μm. To maximize retardance and enhance transmittance for each layer, it is advisable to set pulse density as high as possible within the processing window of type X. The fluctuation in transmittance within the transitional region may be attributed to the disruption of type X modification and the progressive formation of type II modification, necessitating further experimental clarification.

Furthermore, Fig. 3(e) and 3(f) depict the retardance and transmittance maps as functions of pulse energy and pulse density, respectively, with a fixed pulse duration of 450 fs. Notably, type X (highlighted by the dashed box) typically emerges with lower pulse density and energy. Within the processing window for type X, elevating both pulse density and energy yields a greater retardance. However, as the pulse density and/or energy increase further, type X transitions to type II, characterized by higher retardance but lower transmittance. Scanning electron microscopy (SEM) images illustrating the typical laser-induced anisotropic nanostructures for type X and type II are provided in Fig. S7 (Supplementary Information). Type X exhibits abundant elongated nanopores with long-axis sizes ranging from tens to 100 nanometers, while type II showcases nanogratings with enlarged dimensions. Furthermore, it is noteworthy that type II demonstrates higher UV-VIS absorption spectra compared to type X (Fig. S6, Supplementary Information), indicating the presence of a higher concentration of defects within type II. The smaller feature size in type X leads to less scattered light[52], contributing to its higher transmittance.

Since the retardance of single-layer form birefringence for both type II and type X is significantly less than $\lambda/2$, the implementation of multi-layer structures becomes necessary to achieve high conversion efficiency of the metasurface. The spacing between adjacent layers emerges as a critical factor in metasurface preparation. When the interval distance is too small, there is a risk of overwriting the preformed birefringent layer during subsequent layer fabrication and generating random ablation points. This can alter the birefringent optical properties, thus degrading the metasurface performance.

Conversely, an excessively large interval distance can deepen the metasurface, potentially impacting its optical performance due to optical coupling among nanostructures. Figure S8 (Supplementary information) illustrates the relationship between the retardance of three-layer structures and interval distance. The retardance gradually diminishes with larger interval distances due to smaller layer overlapping, stabilizing when the interval distance reaches or exceeds 40 μm. Hence, 40 μm is deemed an appropriate interval distance. Subsequently, during metasurface preparation, the interval distance is set at 40 μm to ensure optimal performance.

Fabrication and characterization of metasurfaces

Following the demonstration of femtosecond laser-induced form birefringence within silica glass, metasurfaces operating at 808 nm were fabricated, depicted in Fig. 4(a) and Fig. 4(b). For type II metasurfaces, laser processing employed parameters of 450 fs, 200 pulses/μm, and 1.1 μJ, while type X metasurfaces were produced with parameters of 450 fs, 33 pulses/μm, and 1.1 μJ. According to the retardance of single-layer form birefringence, four and 20 layers were fabricated for type II and type X metasurfaces, respectively. In addition, there is no difference in the laser processing parameter for fabricating different layers at different depths. The detailed parameters involved in the fabrication of type II and type X metasurfaces are summarized in Table S1 (Supplementary information). To mitigate the influence of polarization direction on femtosecond laser-induced retardance (as illustrated in Fig. S9, Supplementary information), stemming from the inherent anisotropy of laser-material interactions[53,54], consistent scanning direction with the polarization was maintained throughout the fabrication process of metasurfaces. Additionally, for simplicity, the continuous phase of the designed metasurface was segmented into 16 regions (referred to as the multi-level phase), as depicted in Fig. 4(e). Theoretical calculations demonstrate that the optical field modulated by the multi-level phase exhibits nearly identical properties to that modulated by the continuous phase, as shown in Fig. 5(a) and Fig. 5(c).

The images depicting the fast axis angle distribution within the prepared metasurfaces [Fig. 4(c) and Fig. 4(d)] reveal the attainment of a multi-level geometric phase in the azimuthal direction. Moreover, the insert

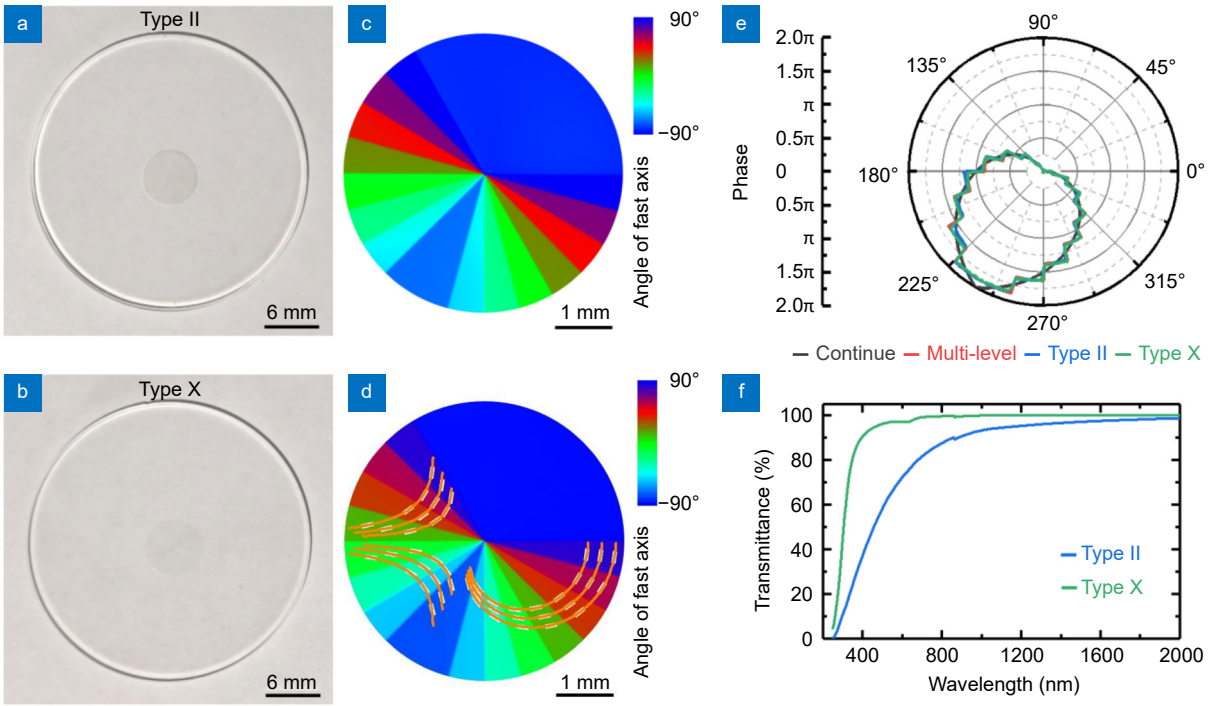

Fig. 4 | Prepared metasurfaces with type II and type X modifications. (**a**, **b**) Photographs of metasurfaces with type II and type X modifications inside silica glass. (**c**, **d**) Images of the fast axis angle of the fabricated metasurfaces.White lines in (d) indicate the fast axis angle of the fabricated birefringent nanostructures. Orange curves in (d) indicate the fast axis angle of the catenary structures. (**e**) Phase evolution in the azimuthal direction of the designed and fabricated metasurfaces. (**f**) Transmission spectra of the two fabricated metasurfaces with reference to pristine silica glass. Transmittance of the type X metasurface is greater than 99.4% in the near-infrared range.

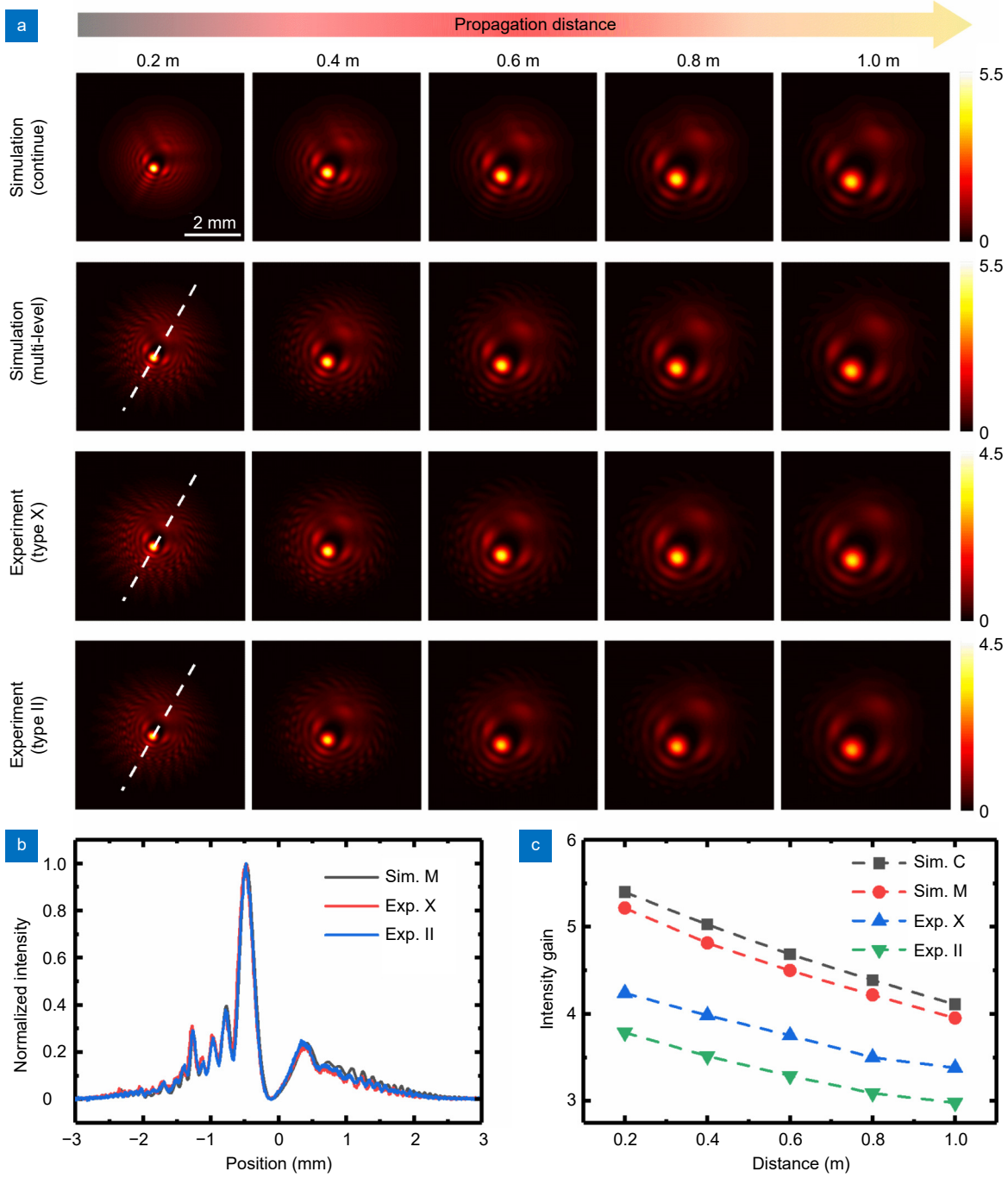

Fig. 5 | Characterization of optical field distribution modulated by the prepared metasurfaces. (**a**) Intensity distribution of the modulated beam along the propagation direction. The simulated patterns modulated by continuous phase and multi-level phase as well as the measured patterns modulated by metasurfaces of type II and type X are compared. (**b**) Normalized intensity distribution along the dashed lines indicated in (a) for both the simulated and measured optical patterns. The normalized intensity of each line is expressed as: $I_{nor}(x_l)= I(x_l)/\max[I(x_l)]$, where $I(x_l)$ is the intensity along the line. (**c**) Intensity gain along the propagation distance.

lines in Fig. 4(d) reveal that these fabricated multi-level structures are the discretization of continuous catenary structures[32]. In principle, more continuous structures would be helpful for the improvement of efficiency. Figure 4(e) provides a quantitative assessment of the measured geometric phases compared to their design counterparts, demonstrating strong consistency. Furthermore, discernible differences in transmission are evident between metasurfaces of type II and type X [Fig. 4(f)]. Generally, type X metasurfaces exhibit higher measured

transmittance across the UV-VIS-NIR spectral regions (250–2000 nm) compared to type II, with the disparity particularly pronounced in the visible and near-infrared spectral range. For instance, at a wavelength of 808 nm, the transmittance reaches 87.9% and 99.6% for type II and type X metasurfaces, respectively.

The metasurfaces exhibit localized optical intensity enhancement across varying propagation distances (0.2 m–1 m), as depicted in Fig. 5. Illuminated by a circularly polarized Gaussian beam with a wavelength of 808 nm, the metasurfaces were analyzed without a co-polarization analyzer during the capture of transmitted intensity distribution via a laser beam profiler. This setup aimed to demonstrate the high conversion efficiency of the fabricated metasurfaces. Experimental intensity distributions modulated by metasurfaces of type II and type X closely mirror simulation results, as evidenced in Fig. 5(a). Notably, an identical distribution of normalized intensity along the dashed line [indicated in Fig. 5(a)] is discernible between the simulated and experimental intensity patterns [Fig. 5(b) and Fig. S10, Supplementary information]. These compelling results attest to the exceptional performance of the fabricated metasurfaces. The measured intensity gain is defined as the ratio of the captured peak intensity of the metasurface-modulated beam to that of the original Gaussian beam. Consistent with simulation outcomes, the measured intensity gain diminishes progressively with increasing propagation distance, as shown in Fig. 5(c). Metasurfaces of type II and type X achieve intensity gains of 3.0 and 3.4 at the propagation of 1 m, respectively. It is noteworthy that the measured intensity gain for metasurfaces falls short of the simulation results. In the current experimental setup, the metasurfaces lack antireflective films on the front and rear surfaces of silica glass, resulting in additional transmission loss due to the reflection of pristine silica glass, in addition to the transmission loss of form birefringence. This combined transmission loss contributes to the observed decline in measured intensity gain. For metasurfaces of type X, where the transmittance of birefringent modification approaches unity, the primary transmission loss arises from the reflection of pristine silica glass. Consequently, a higher measured intensity gain is attained with metasurfaces of type X. Furthermore, other factors contributing to the difference between measured and simulated results include the imperfections in the incident Gaussian beam and slight geometric phase deviations, which may impact the generation of multiple collinear vortex beams and attenuate the corresponding superposition effect.

To showcase the resistance of the prepared metasurfaces against intense laser exposure, we assessed their LIDTs using the standardized 1-on-1 method outlined in ISO 21254. The testing apparatus utilized a laser with a wavelength of 1064 nm and a pulse duration of 6 ns. The LIDT, denoting the threshold at which damage occurs with 0% probability, is 18.7 J/cm^2 for the metasurface of type II [Fig. 6(a)]. Notably, the metasurface of type X exhibits a substantially higher LIDT of 68.0 J/cm^2 [Fig. 6(b)]. This significant variance in LIDT values can be attributed to laser-induced defects within the modification region. In comparison to type X, the femtosecond laser-induced modification process for type II is more aggressive due to the cumulative effect of more laser pulses. Consequently, it generates a greater density of defects during the formation of birefringent nanograttings (Fig. S6, Supplementary information). These defects serve as energy absorbers, facilitating the deposition of pulse energy during intense laser exposure and ultimately reducing the LIDT. Therefore, metasurfaces with excellent

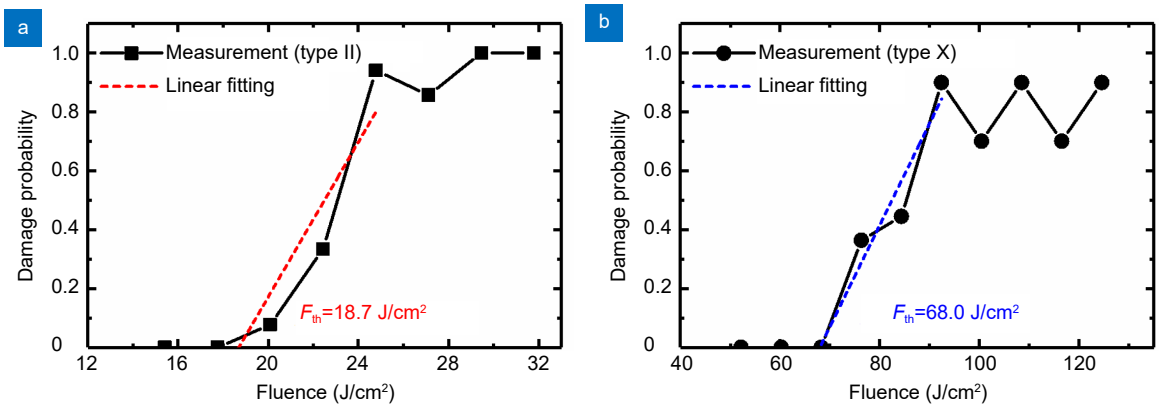

Fig. 6 | LIDT of the prepared metasurfaces with (**a**) type II and (**b**) type X birefringent nanostructures.

performance of beam modulation and high LIDT have been verified based on the characterization results shown in Fig. 5 and Fig. 6.

Conclusions

In summary, a single geometric metasurface based on a sliced phase pattern in the azimuthal direction is proposed and experimentally demonstrated to generate MCVBs with equally spaced OAM topological charge (l) for enhancing the vortex field. The phase-only modulation strategy enables high conversion efficiency for MCVBs generation. Moreover, the geometric metasurface has been fabricated by utilizing femtosecond laser-induced birefringent nanostructure embedded in silica glass, which shows outstanding properties of high transmittance, high damage threshold, and high conversion efficiency. This method is maskless, accessible, and flexible. As a proof of the concept, a single optical hot spot with the intensity gain larger than 3.4 within a propagation distance of 1 m is experimentally demonstrated and compared with calculation values. In addition, transmittance greater than 99.4% in the near-infrared ranges and LIDT as high as 68.0 J/cm^2 (at 1064 nm, 6 ns) are experimentally verified. Such LIDT is much higher than that of conventional metasurfaces, e.g. titanium dioxide-based metasurfaces. The demonstrated high-threshold metasurface shows promising prospects in a host of high-power laser systems. To improve the fabrication efficiency of such metasurfaces, spatial beam shaping (e.g. multi-focus beam) will be applied to increase the retardance of form birefringence induced by a single scanning process.

Materials and methods

Fabrication of form birefringence and metasurfaces

Laser-induced form birefringence in silica glass (Corning 7980) was realized by progressive scanning of the femtosecond laser. The femtosecond laser was focused 200 μm below the surface of silica glass by an objective (10×, NA = 0.26). The fabrication process was carried out by a homemade femtosecond laser machining system which can control the laser parameters and 3-axial translation stage (Fig. S5, Supplementary information). The femtosecond laser was generated by a Yb-doped potassium gadolinium tungstate (Yb:KGW)-based mode-locked regenerative amplified femtosecond laser system (PH2-20, Light Conversion Ltd.). The central wavelength is 1030 nm, while the pulse duration (220 fs–10 ps) and repetition rate (1 kHz–1 MHz) are variable. The pulse energy was tuned by an optical attenuator consisting of a half-wave plate (HWP1) and a polarizing beamsplitting cube. The polarization direction was controlled by another half-wave plate (HWP2). The repetition rate was set at 205 kHz while the pulse duration ranged from 220 fs to 700 fs. Since the repetition rate was constant, the pulse density was tuned by changing the velocity of the translation stage. The interval of each scanning line was set at 1 μm. The interval-distance of layers was set at 40 μm for the fabrication of metasurfaces.

Morphology characterization

To analyze the morphologies of laser-induced birefringent nanostructures, the sample was polished and then etched in 1 mol/L KOH solution for 24 hours. The exposed nanostructures were imaged with scanning electron microscopy (Helios 5 CX, Thermo Scientific).

Optical characterization

The retardance and angle of the fast axis of laser-modified regions were quantitatively measured through a commercial birefringence imaging microscope (Exicor® MicroImagerTM, Hinds Instruments). The transmittance was obtained by a microscope (BX53M, Olympus) equipped with a spectrograph (Nova-ex, Ideaoptics). The transmission spectrum and absorption spectrum of the prepared metasurfaces were measured by a UV-VIS-NIR spectrometer (Lambda 1050, PerkinElmer). For verifying the light field modulation capability of the fabricated metasurfaces, the metasurfaces were illuminated by a circularly polarized Gaussian beam with a wavelength of 808 nm at normal incidence. The modified light fields after the metasurface were directly captured by a laser beam profiler (Beamage-4M, Gentec-eo) located at different propagation distances. As a comparison, the intensity distributions of the Gaussian beam at corresponding propagation distances were captured as well.

LIDT test

The LIDTs of the prepared metasurfaces were measured by a standard 1-on-1 method according to ISO 21254. The wavelength and pulse duration of the test system laser are 1064 nm and 6 ns, respectively. The damage probability under different laser fluencies was calculated. The relationship between the damage probability and the laser fluence was linearly fitted to get the damage threshold of 0% probability. The damage threshold of 0% probability was the LIDT (1-on-1) of the metasurface.

References

1. Allen L, Beijersbergen MW, Spreeuw RJC et al. Orbital angular momentum of light and the transformation of Laguerre-Gaussian laser modes. *Phys Rev A* **45**, 8185–8189 (1992).
2. Yao AM, Padgett MJ. Orbital angular momentum: origins, behavior and applications. *Adv Opt Photonics* **3**, 161–204 (2011).
3. Shen YJ, Wang XJ, Xie ZW et al. Optical vortices 30 years on: OAM manipulation from topological charge to multiple singularities. *Light Sci Appl* **8**, 90 (2019).
4. Zhang TC, Dong KC, Li JC et al. Twisted moiré photonic crystal enabled optical vortex generation through bound states in the continuum. *Nat Commun* **14**, 6014 (2023).
5. Apurv Chaitanya N, Aadhi A, Jabir MV et al. Frequency-doubling characteristics of high-power, ultrafast vortex beams. *Opt Lett* **40**, 2614–2617 (2015).
6. Ivanov M, Thiele I, Bergé L et al. Intensity modulated terahertz vortex wave generation in air plasma by two-color femtosecond laser pulses. *Opt Lett* **44**, 3889–3892 (2019).
7. Hamazaki J, Morita R, Chujo K et al. Optical-vortex laser ablation. *Opt Express* **18**, 2144–2151 (2010).
8. Ma HX, Li XZ, Tai YP et al. Generation of circular optical vortex array. *Ann Phys* **529**, 1700285 (2017).
9. Tian YH, Wang LL, Duan GY et al. Multi-trap optical tweezers based on composite vortex beams. *Opt Commun* **485**, 126712 (2021).
10. Anguita JA, Herreros J, Djordjevic IB. Coherent multimode OAM superpositions for multidimensional modulation. *IEEE Photonics J* **6**, 7900811 (2014).
11. Xie GD, Liu C, Li L et al. Spatial light structuring using a combination of multiple orthogonal orbital angular momentum beams with complex coefficients. *Opt Lett* **42**, 991–994 (2017).
12. Zhu L, Wang J. Simultaneous generation of multiple orbital angular momentum (OAM) modes using a single phase-only element. *Opt Express* **23**, 26221–26233 (2015).
13. Huang SJ, Miao Z, He C et al. Composite vortex beams by coaxial superposition of Laguerre-Gaussian beams. *Opt Lasers Eng* **78**, 132–139 (2016).
14. Zhang YX, Pu MB, Jin JJ et al. Crosstalk-free achromatic full Stokes imaging polarimetry metasurface enabled by polarization-dependent phase optimization. *Opto-Electron Adv* **5**, 220058 (2022).
15. Xie X, Pu MB, Jin JJ et al. Generalized pancharatnam-berry phase in rotationally symmetric meta-atoms. *Phys Rev Lett* **126**, 183902 (2021).
16. Zhang F, Pu MB, Luo J et al. Symmetry breaking of photonic spin-orbit interactions in metasurfaces. *Opto-Electron Eng* **44**, 319–325 (2017).
17. Luo XG, Zhang F, Pu MB et al. Catenary optics: a perspective of applications and challenges. *J Phys Condens Matter* **34**, 381501 (2022).
18. Luo XG. Subwavelength artificial structures: opening a new era for engineering optics. *Adv Mater* **31**, 1804680 (2019).
19. Liu WW, Li ZC, Ansari MA et al. Design strategies and applications of dimensional optical field manipulation based on metasurfaces. *Adv Mater* **35**, 2208884 (2023).
20. Zhang F, Pu MB, Li X et al. Extreme-angle silicon infrared optics enabled by streamlined surfaces. *Adv Mater* **33**, 2008157 (2021).
21. Ossiander M, Meretska ML, Hampel HK et al. Extreme ultraviolet metalens by vacuum guiding. *Science* **380**, 59–63 (2023).
22. Liu XY, Zhang JC, Leng BR et al. Edge enhanced depth perception with binocular meta-lens. *Opto-Electron Sci* **3**, 230033 (2024).
23. Fu JC, Jiang MT, Wang Z et al. Supercritical metalens at h-line for high-resolution direct laser writing. *Opto-Electron Sci* **3**, 230035 (2024).
24. Li X, Chen LW, Li Y et al. Multicolor 3D meta-holography by broadband plasmonic modulation. *Sci Adv* **2**, e1601102 (2016).
25. Overvig AC, Shrestha S, Malek SC et al. Dielectric metasurfaces for complete and independent control of the optical amplitude and phase. *Light Sci Appl* **8**, 92 (2019).
26. Fu R, Chen KX, Li ZL et al. Metasurface-based nanoprinting: principle, design and advances. *Opto-Electron Sci* **1**, 220011 (2022).
27. Guo YH, Zhang SC, Pu MB et al. Spin-decoupled metasurface for simultaneous detection of spin and orbital angular momenta via momentum transformation. *Light Sci Appl* **10**, 63 (2021).
28. Zang HF, Zhang ZY, Huang ZT et al. High-precision two-dimensional displacement metrology based on matrix metasurface. *Sci Adv* **10**, eadk2265 (2024).
29. Zhang YX, Jin JJ, Pu MB et al. Ultracompact metasurface for simultaneous detection of polarization state and orbital angular momentum. *Laser Photonics Rev* **18**, 2301012 (2024).
30. Arbabi A, Horie Y, Bagheri M et al. Dielectric metasurfaces for complete control of phase and polarization with subwavelength spatial resolution and high transmission. *Nat Nanotechnol* **10**, 937–943 (2015).
31. Dorrah AH, Rubin NA, Zaidi A et al. Metasurface optics for on-demand polarization transformations along the optical path. *Nat Photonics* **15**, 287–296 (2021).
32. Pu MB, Li X, Ma XL et al. Catenary optics for achromatic generation of perfect optical angular momentum. *Sci Adv* **1**, e1500396 (2015).
33. Zhang F, Zeng QY, Pu MB et al. Broadband and high-efficiency accelerating beam generation by dielectric catenary metasurfaces. *Nanophotonics* **9**, 2829–2837 (2020).
34. Liu MZ, Huo PC, Zhu WQ et al. Broadband generation of perfect Poincaré beams via dielectric spin-multiplexed metasurface. *Nat Commun* **12**, 2230 (2021).
35. Georgi P, Wei QS, Sain B et al. Optical secret sharing with cascaded metasurface holography. *Sci Adv* **7**, eabf9718 (2021).
36. Zhang F, Guo YH, Pu MB et al. Meta-optics empowered vector visual cryptography for high security and rapid decryption. *Nat Commun* **14**, 1946 (2023).
37. Zheng CL, Wang GC, Li J et al. All-dielectric metasurface for manipulating the superpositions of orbital angular momentum via spin-decoupling. *Adv Opt Mater* **9**, 2002007 (2021).
38. Ahmed H, Intaravanne Y, Ming Y et al. Multichannel superposition of grafted perfect vortex beams. *Adv Mater* **34**, 2203044 (2022).
39. Ming Y, Intaravanne Y, Ahmed H et al. Creating composite vortex beams with a single geometric metasurface. *Adv Mater* **34**, 2109714 (2022).
40. Kai Y, Lem J, Ossiander M et al. High-power laser beam shaping using a metasurface for shock excitation and focusing at the microscale. *Opt Express* **31**, 31308–31315 (2023).
41. Xie LH, Tao RM, Guo C et al. High-power cylindrical vector beams generated from an all-fiber linearly polarized laser by metasurface extracavity conversion. *Appl Opt* **60**, 7346–7350

(2021).
42. Wu QY, Zhou JX, Chen XY et al. Single-shot quantitative amplitude and phase imaging based on a pair of all-dielectric metasurfaces. *Optica* **10**, 619–625 (2023).
43. Xu DY, Xu WH, Yang Q et al. All-optical object identification and three-dimensional reconstruction based on optical computing metasurface. *Opto-Electron Adv* **6**, 230120 (2023).
44. Sakakura M, Lei YH, Wang L et al. Ultralow-loss geometric phase and polarization shaping by ultrafast laser writing in silica glass. *Light Sci Appl* **9**, 15 (2020).
45. Shayeganrad G, Chang X, Wang HJ et al. High damage threshold birefringent elements produced by ultrafast laser nanostructuring in silica glass. *Opt Express* **30**, 41002–41011 (2022).
46. Yan Y, Yue Y, Huang H et al. Multicasting in a spatial division multiplexing system based on optical orbital angular momentum. *Opt Lett* **38**, 3930–3933 (2013).
47. D'Errico A, D'Amelio R, Piccirillo B et al. Measuring the complex orbital angular momentum spectrum and spatial mode decomposition of structured light beams. *Optica* **4**, 1350–1357 (2017).
48. Fu SY, Zhai YW, Zhang JQ et al. Universal orbital angular momentum spectrum analyzer for beams. *PhotoniX* **1**, 19 (2020).
49. Huo PC, Yu RX, Liu MZ et al. Tailoring electron vortex beams with customizable intensity patterns by electron diffraction holography. *Opto-Electron Adv* **7**, 230184 (2024).
50. Luo XG. Principles of electromagnetic waves in metasurfaces. *Sci China Phys Mech Astron* **58**, 594201 (2015).
51. Mishchik K, D'Amico C, Velpula PK et al. Ultrafast laser induced electronic and structural modifications in bulk fused silica. *J Appl Phys* **114**, 133502 (2013).
52. Cox AJ, DeWeerd AJ, Linden J. An experiment to measure Mie and Rayleigh total scattering cross sections. *Am J Phys* **70**, 620–625 (2002).
53. Shimotsuma Y, Sakakura M, Kazansky PG et al. Ultrafast manipulation of self-assembled form birefringence in glass. *Adv Mater* **22**, 4039–4043 (2010).
54. Lei YH, Wang HJ, Skuja L et al. Ultrafast laser writing in different types of silica glass. *Laser Photonics Rev* **17**, 2200978 (2023).

Acknowledgements

We are grateful for financial supports from the National Key Research and Development Program (Grant No. 2018YFA0701800), the National Natural Science Foundation of China (NSFC) (Grant No. 62192773), and the West Light Foundation of Chinese Academy of Sciences (Grant No. xbzg-zdsys-202307).

Author contributions

X.G.L. and X.L. proposed the original idea and supervised the project. Q.S. Wang and Y.F. designed, fabricated and characterized all the samples. Y.M. and H.H. helped the sample measurements. All authors involved in the discussion and analysis of the data and results. Q.S.W., Y.F., and X.L. wrote the manuscript. All authors commented on the manuscript.

Competing interests

Xiangang Luo and Mingbo Pu serve as an Editor for the Journal, and no other author has reported any competing interests.

Supplementary information

Supplementary information for this paper is available at
https://doi.org/10.29026/oea.2024.240112

Scan for Article PDF